Measurements of contact angles of water on Al-based intermetallic surfaces

Measurements of contact angles of water on Al-based intermetallic surfaces

J M Dubois[1,4]**, V Fournée**[2,5]**, P A Thiel**[2] **and E Belin-Ferré**[3]

[1] Institut Jean Lamour (FR2797 CNRS-INPL-UHP), Nancy Université, Ecole des Mines,
Parc de Saurupt, F-54042 Nancy, France
[2] Ames Laboratory, Iowa State University, Ames, IA 50011, USA
[3] LCPMR (CNRS UMR 7614), Université P M Curie, 11 Rue Pierre et Marie Curie,
F-75231 Paris, France

E-mail: dubois@mines.inpl-nancy.fr

Abstract

A systematic study was performed of the contact angle of minute droplets of water deposited on various aluminium-based intermetallics in ambient conditions. The dataset was complemented by measurements of electronic partial densities of states and oxide layer thicknesses. We studied a broad variety of specimens, ranging from simple cubic, CsCl-type phases to quasicrystals and high-order approximants. The thickness of the oxide layer, that is always present in air, was varied between 2 and more than 10 nm. Within these limits, the contact angle varies considerably and, surprisingly, decreases with increasing thickness of the oxide dielectric. Furthermore, it is clearly the highest on samples that show the largest crystal complexity, i.e. quasicrystals.

It follows that the reversible adhesion energy directly deduced from contact angle is essentially controlled by the (squared) density of states at Fermi energy in the bulk of the sample and the inverse of the (squared) thickness of the native oxide film at the surface of the material. We interpret these results in terms of electrostatic image forces developed in the conduction cloud by the dipoles of the water molecules.

(Some figures in this article are in colour only in the electronic version)

1. Introduction

The science of wetting a flat surface by a small enough droplet of liquid (so that gravity plays no role) is an ancient part of thermodynamics that is often considered a self-contained part of science[6]. It is nowadays admitted that the equilibrium shape of the droplet results from the balance of the surface tensions shown in figure 1, which obeys Young's equation [2]:

$$\gamma_{SV} = \gamma_L \cos\theta + \gamma_{SL}. \qquad (1)$$

Here, the terms γ_L, γ_{SV}, γ_{SL} define, respectively, the surface tension of the liquid, the surface tension of the solid (in the presence of the liquid vapour) and the interfacial tension between solid and liquid. This equation is valid only if the
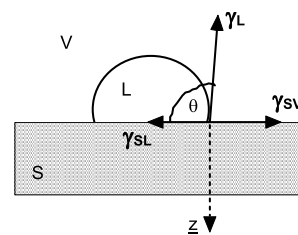

Figure 1. Equilibrium shape of a small liquid droplet (L) deposited on a flat solid surface (S) in the presence of its vapour (V). The contact angle θ results from the balance at the position of the three-phase line of the surface tensions characteristic of the three L–S, S–V and L–V interfaces and reaction of the solid shown as a dashed arrow along the z direction.

contact angle is well defined, a situation that does not occur if equilibrium is not reached, or equivalently, if the film pressure is too large (see below). Furthermore, the exact mechanical
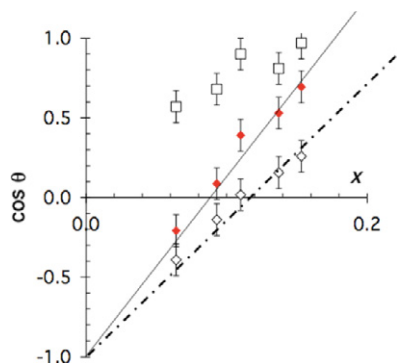
---

[4] Author to whom any correspondence should be addressed.
[5] Present address: Institut Jean Lamour, Nancy Université, Parc de Saurupt, F-54042 Nancy, France.
[6] Literature on this subject is abundant, see, for instance, [1].

1

Figure 2. Comparison between the variation of $y = \cos\theta$ versus $x = 2\sqrt{\gamma_L^{LW}}/\gamma_L$ measured for a sample of Teflon (open diamonds and dashed line), a sample of bulk alumina (squares, no line) and the freshly polished surface of a multi-grained $Al_{59}B_3Cu_{25.5}Fe_{12.5}$ icosahedral quasicrystal (solid diamonds and thin solid line). The vertical bars represent the scatter of at least ten different measurements. The liquids used are (from left to right on the abscissa axis) water, glycerol, ethylene glycol, diiodomethane and tricresylphosphate. Observe that the thin and dashed lines go to $\cos\theta = -1$ for $x = 0$, as expected when no polar contribution is present at the solid surface. This is not the case with bulk alumina, as demonstrated by the strong shift of the data from linearity, except for the last two liquids, that are apolar.

equilibrium involves a term (shown by a vertical dashed arrow in figure 1), which represents the reaction of the solid surface to the forces induced by the presence of the droplet. This term is usually omitted in equation (1).

Surface tensions act on the three-phase line that defines the separation between solid surface, liquid and vapour of the liquid. In the context of the present paper, we may identify the surface tensions with the surface energies, respectively, of the solid, the liquid and the solid–liquid interface. We show in the following that the film pressure of the liquid is negligible for the samples of interest herein. Therefore, we shall also admit that the surface energy of the solid in the presence of the liquid is equal to the true surface energy of the solid, i.e. $\gamma_S \equiv \gamma_{SV}$. Nevertheless, we insist here on the fact that all solids considered hereafter are intermetallic samples equipped with their native oxide, since all experiments are done in ambient atmosphere at room temperature.

When a droplet of water is placed on a freshly prepared surface of a quasicrystal, the droplet does not spread, but rather it 'beads up'. This behaviour, first observed empirically, [3] may be put on a quantitative basis by measuring the contact angle, θ, a set of data that was already reported elsewhere [4, 5]. Quasicrystals display anomalously large values of θ ($90° < \theta < 110°$), whereas pure aluminium metal shows values around $60°$–$70°$, even though both are covered by the same surface oxide under the conditions of the experiment.

A more specific physical insight can be gained by using several liquids of variable surface energy components, as is explained in the following (section 2). This method allows us to investigate separately the Lifshitz–van der Waals (LW) contribution (or dispersive term γ_L^{LW}) and other contributions (labelled 'polar' hereafter for simplicity) to the surface energy

of the solid, essentially the Lewis acid–base (AB) interactions[7]. A solid like PTFE (Teflon®), which shows no polar component whatsoever, produces a linear variation of $y = \cos\theta$ when plotted against $x = 2\sqrt{\gamma_L^{LW}}/\gamma_L$ (see equation (5)). This is not observed, as shown in figure 2, on bulk alumina, and also not on the pure and necessarily oxidized aluminium metal, both of which present a significant shift from linearity (and are relevant to the present study since both aluminium metal and quasicrystals are covered with the same amorphous alumina layer).

The traditional interpretation of this wetting behaviour of the bulk oxide is based upon the presence at the very surface of electrostatic charges and of chemical interactions with the liquid. A coupling between polar components carried, respectively, by the liquid molecules and the solid surface explains the shift from linearity (again, see equation (5) hereafter) and simultaneously marks clearly the presence of such a polar contribution at the solid surface. Conversely, as observed on Teflon, linearity of the plot that goes to $y = \cos\theta = -1$ when $x = 2\sqrt{\gamma_L^{LW}}/\gamma_L = 0$ definitely makes sure that polar components are absent at the solid surface.

Compared to Teflon and alumina, as demonstrated in figure 2, a quasicrystal of high lattice quality shows a variation of $\cos\theta$ with the selected liquids that is very close to linear, like Teflon, and departs from the plot obtained with a sample of single-crystalline alumina in a definite and clearly visible way. This indicates that if any polar contribution is present at the surface of this specific quasicrystal prepared according to the protocol described in the coming section, it must be very small on the one hand, and on the other hand, much smaller than the one expected from the covering oxide.

Accordingly, the motivation of our study was to understand better the atypical behaviour of contact angles measured between minute droplets of ultra-pure water and mirror-polished samples of quasicrystals. It turned out that more light could be shed on this issue by studying a large variety of specimens, including metals, oxides and crystalline compounds of the same Al–TM (TM = one or several transition metals) family. The evidence, illustrated above, that the oxide layer that covers all Al-based samples (and metals as well) in ambient conditions does not play the role expected from a study of the pure oxide alone has led us to seek for interactions arising from beyond the oxide layer, in contrast to expectations found in the literature that base their interpretation solely on the extreme surface of the oxide [7]. Therefore, we have also carefully studied the role played by the thickness of the oxide layer and by the electronic interactions in the solid, respectively. A large number of Al-based intermetallics was studied, some of them being equipped by an artificial layer of pure and amorphous alumina, in order to vary extensively the experimental parameters.

---

[7] See this article for references to Bronsted, Lewis and others regarding the theory of contact angles and wetting by liquids. Note that we use the term 'wetting' in a broad sense, to encompass the entire range of behaviour—contact angles—that can describe the interaction of a liquid droplet with a solid [6].

2. Theoretical background

Based on the existence of a marked pseudo-gap in the electronic density of states (DOS) of most quasicrystals known so far, Rivier [8] suggested that the reduced wetting observed on quasicrystals could be due to a combined effect of surface thermodynamics, including pinning due to roughness, and reduced frequency of chemical bonds at the surface. However, this theoretical approach ignored the oxide layer always present at the surface of a quasicrystal studied in ambient air and could not have predicted the observations summarized in figure 2. Therefore, we develop hereafter another approach.

The reversible adhesion energy of the liquid on the solid surface is the difference between the surface energies of the two free surfaces before and after wetting, namely

$$W_L = \gamma_S + \gamma_L - \gamma_{SL}. \tag{2}$$

The term W_L may be evaluated assuming a two-step reversible process. First, the droplet is separated from the solid surface with no area change. Second, the droplet is re-deposited on the solid after its contact area is changed by a quantity equivalent to the one imposed by the contact with the solid. This leads to a free energy variation, which cancels out after reaching the equilibrium shape, hence

$$W_L = \gamma_L(1 + \cos\theta) + \Pi \tag{3}$$

with $\Pi = \gamma_{SL} - \gamma_{SV}$, the film pressure that represents the influence of vapour adsorption on the solid. This latter term is often not negligible and induces an ill-defined contact angle. With the solids considered hereafter, however, the angle θ is well defined with values ranging close to or above 80°–90°. Hence, the solid surface energy is comparable to or smaller than that of the liquids so that the film pressure is negligible (except for alumina, window glass and oxidized pure metals). It is then appropriate to separate the contribution to W_L that arises from instantaneous, or dispersive (LW), charge distributions from the ones associated with the Lewis acid–base (AB) behaviour of the surface due to possible charges trapped at or extracted from the surface [6] (see footnote 7):

$$W_L = I_{SL}^{LW} + I_{SL}^{AB}. \tag{4}$$

Furthermore, we may split each contribution according to a geometric mean rule [6] (see footnote 7) into components coming from the liquid on the one hand and from the solid on the other. Hence, combining equations (1) and (3), and with a negligible film pressure:

$$W_L = \gamma_L(1 + \cos\theta) = 2(\gamma_S^{LW}\gamma_L^{LW})^{1/2} + I_{SL}^{AB}. \tag{5}$$

The Lewis AB interactions are usually split into acid and base parameters of the liquid and solid surface, noted respectively γ_i^+ and γ_i^- (i = S or L), in such a way that

$$\gamma_i^{AB} = 2\sqrt{\gamma_i^+ \gamma_i^-} \tag{6}$$

and

$$I_{SL}^{AB} = 2\left(\sqrt{\gamma_S^+} - \sqrt{\gamma_L^+}\right)\left(\sqrt{\gamma_S^-} - \sqrt{\gamma_L^-}\right). \tag{7}$$

In the absence of AB interactions, either because the liquid is apolar or because the surface shows no permanent polarization, equation (5) produces a linear variation of $y = \cos\theta$ versus $x = 2\sqrt{\gamma_L^{LW}}/\gamma_L$ as shown in figure 2 for the case of Teflon. More specifically, one deduces from the comparison presented in this figure that the quasicrystal surface must be either apolar or monopolar, and also that the film pressure is indeed negligible since $\cos\theta$ goes to -1 for $x = 2\sqrt{\gamma_L^{LW}}/\gamma_L = 0$ for both PTFE and quasicrystal. As stated already, the reason why this specific behaviour occurs on quasicrystals cannot be interpreted on the basis of published literature [1, 6] (see footnotes 6 and 7).

3. Experimental details

Henceforth, we have prepared a large number of solid samples in order to better understand the atypical wetting behaviour of quasicrystals against water. The compositions were selected in the Al–Cu–Fe, Al–Cr–Fe and Al–Pd–Mn systems, known to form stable icosahedral quasicrystals [9] as well as approximant crystals [10] in addition to conventional crystals like the β-Al–(Cu, Fe) B2-cubic phase and the monoclinic λ-Al$_{13}$Fe$_4$ and η-AlCu or tetragonal ω-Al$_7$Cu$_2$Fe and ϕ-Al$_{10}$Cu$_{10}$Fe compounds [11] or the orthorhombic and γ-brass-type Al–Cr–Fe compounds [12]. For comparison, we have also studied reference materials like the pure aluminium metal, pure copper, stainless and low carbon steels and of course Teflon, single-crystalline cubic alumina and a specimen of window glass. We also used an icosahedral Al–Pd–Mn monodomain specimen prepared by the Czochralski pulling technique and annealed in ultra-high vacuum for 2800 h at 800 °C. All other intermetallic compounds were synthesized from crushed or atomized powders and sintered under either uniaxial or high isostatic pressure as described elsewhere [13]. All these specimens contained no detectable porosity. The purity of the single phase present in each specimen was controlled by powder x-ray diffraction and conventional optical microscopy. Their surfaces were large enough to allow for a sufficient number of contact angle measurements to obtain statistical reliability.

All samples were carefully polished down to a mirror finish using exclusively purified water as a lubricant, in order that no organic liquid may be trapped in surface defects of the samples. The final polish was performed with a 4000-grade corundum abrasive paper. Each specimen was then dried in blowing air and immediately placed in the evacuated vessel for 24 h. A liquid nitrogen trap was placed between the pump and the vessel so that no refluxing oil could contaminate the surface. Repeated contact angle measurements over several years have shown that this method yields very reproducible data.

The contact angle measured on an Al-based intermetallic specimen increases with the time elapsed at room temperature in ambient air after polishing the surface under pure water and drying it in a flux of pressurized air for 3 min (figure 3). Comparatively, a sample of bulk alumina of similar surface roughness, prepared in the same conditions, shows almost no
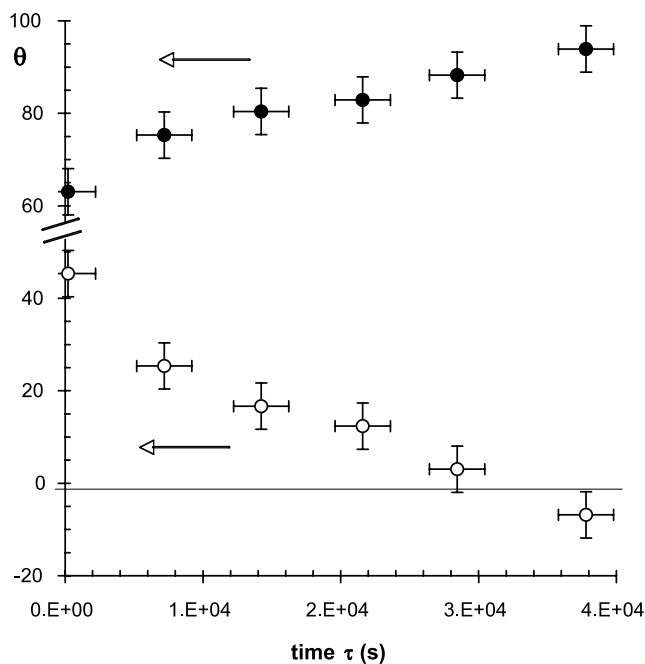
Figure 3. Change of the contact angle θ (top part) and $\cos\theta$ (bottom part) versus time elapsed in ambient air after polishing in pure water a sintered sample of orthorhombic Al–Cu–Fe–Cr approximant of the decagonal phase.

Figure 4. RMS roughness assessed by AFM after polishing to the ultimate 4000-grade corundum paper in water and drying under primary vacuum as explained in the text. The data are shown according to the Vickers hardness (load 0.5 N) of the samples. The group of data for Al-based compounds is denoted as CMAs (complex metallic alloys).

change of the (smaller) contact angle. Contamination of the surfaces by organic molecules, which is easily detected by XPS, cannot account for such a difference between the two kinds of specimens since they were both held in the same atmosphere and measured in the same conditions. It can also not be related to the formation of the native oxide layer, which is very rapidly grown as soon as contact with air is established in comparison to the duration of the contact angle data acquisition [14]. We postulate that the decrease of the wetting behaviour, which is pointed out by the increase of the contact angle, is produced by the slow desorption of the water molecules trapped at the surface within the oxide defects (this proves also that polar interactions have vanished at the surface, thanks to the preparation method used to polish the samples). As explained above, this is the reason why all data reported on in the following were obtained with samples kept in vacuum prior to measurements of θ so as to fully eliminate all traces of water present at the surface before contact angle measurements.

The thickness (denoted as t) of the oxide was measured either by ellipsometry [15] or was derived from an analysis of XPS peaks according to the standard procedure of Strohmeier [16]. Most values of the oxide thickness were found in the range 2–6 nm, except for samples that were corroded intentionally in boiling water, for instance. Those specimens exhibited much thicker oxide layers ($t \gg 10$ nm), all associated with contact angles of water characteristic of bulk alumina, irrespective of the nature of the bulk material underneath the oxide. In strong contrast, values of the contact angle measured on thinner oxide layers ($t < 10$ nm) were found much larger (i.e. above 70° and close to or larger than 90°) and changing with the composition of the intermetallics.
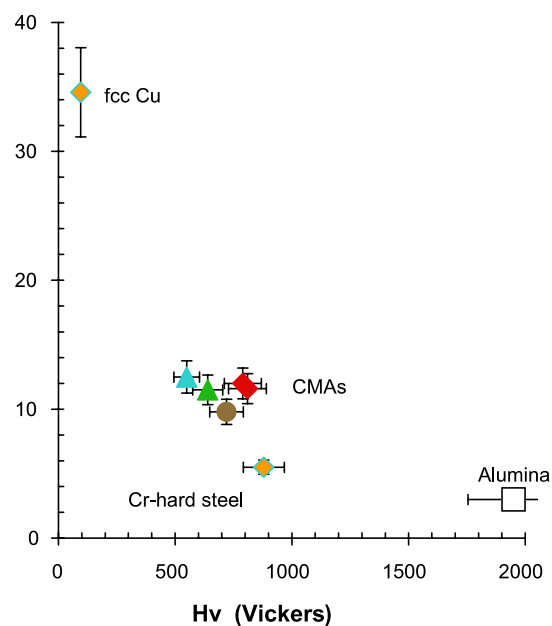
In order to expand the thickness of the oxide from the range 2–6 nm up to $t \cong 10$–12 nm, we have artificially equipped some specimens with a supplementary layer of oxide. The layer was produced by flash evaporation of aluminium on the polished surface of the sample, followed by *in situ* oxidation. A chamber with residual vacuum below 10^{-8}–10^{-9} mbar was used to this end. Several successive steps were necessary to prepare the thickest oxides. Note that this preparation process preserves the Al_2O_3 composition of the top oxide, irrespective of the substrate nature as well as of the composition of the native oxide.

Roughness of all specimens was assessed by AFM and found independent from the sample nature as long as the hardness was within the range 400–800 Vickers units, which holds for all Al-based specimens (figure 4). Of course, softer or harder materials, like Teflon, Cr-steel or pure alumina, showed different roughness after the end of the polish sequence. As a consequence, no correlation was found between contact angle measurements and surface roughness, provided the final polish was the one indicated above. Conversely, surfaces of poorer final polish proved to be more sensitive to surface preparation details and showed contact angles depending on roughness. For instance, figure 5 shows two sets of θ data recorded by visualizing the droplet in the direction of the polishing paper movement, and perpendicular to it. Clearly, the two sets of values coincide only for the best polish, with the smallest roughness characterized by an RMS value below RMS = 10–12 nm.

For the same range of roughness, $10 < $ RMS < 12 nm, we could assess that receding and advancing contact angles are identical, within experimental precision. Throughout the
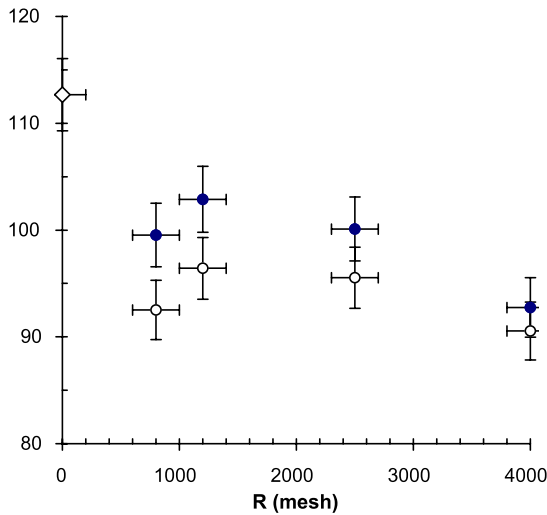
Figure 5. Contact angle of ultra-pure water deposited on a sample of orthorhombic Al–Cu–Fe–Cr compound and viewed perpendicular (solid dots) and parallel (open dots) to the polishing direction, using corundum abrasive paper of increasing mesh size (x axis).
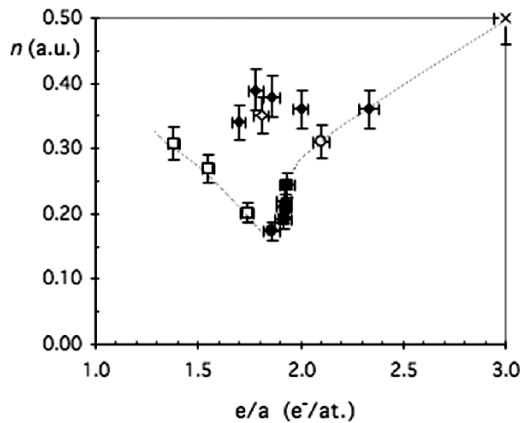

Figure 6. Plot of the intensity n of the Al 3p distribution at the Fermi level against the electron to atom ratio e/a in a series of conventional Al–Cu(Fe) crystals (open and full diamonds), Al–Cu–Fe β-phases (open squares) and icosahedral Al–Cu–Fe compounds (lowest filled dot) and approximants (full squares). The x axis is labelled according to the average electron per atom ratio, assuming that Al carries a valence of $3e^-$, Cu $1e^-$ and Fe a negative valence of $-2e^-$.

present study, all data were collected by depositing at least 10 droplets and taking the average between contact angle data measured on both sides of the droplet. A standard commercial apparatus (Digidrop® from GBX Company, France) was used to this end, continuously recording the image of the droplet while evaporation of water at room temperature proceeded. The initial contact angle at equilibrium was obtained from image records by considering only the first few tens of seconds of recording.

Finally, the Al 3p partial density of states in each Al-based intermetallic sample was deduced from x-ray emission spectroscopy measurements as explained elsewhere [16]. Accurate position of the Fermi level on the binding energy scale was obtained afterwards from XPS studies of carbon
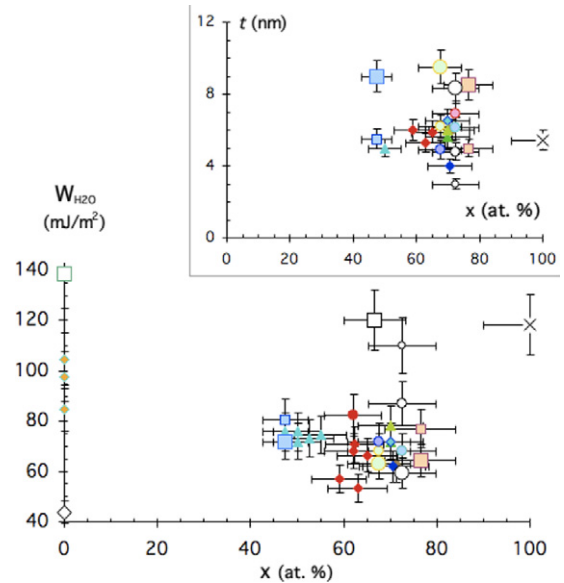

Figure 7. Reversible adhesion energy W_{H_2O} of ultra-pure water deposited on the solids described in the text. The x axis gives the Al concentration in the $Al_x TM_{1-x}$ specimens (where TM stands for one or several transition metals alloyed with Al, or for oxygen in Al_2O_3 alumina), while materials that contain no aluminium (Teflon, steel, fcc Cu, window glass) are arbitrarily set at $x = 0$. The inset shows the thickness t of the alumina oxide layer found at the surface of the Al-based specimens. Note that the same symbols are used in both parts of the figure, knowing that a larger symbol goes with a thicker layer. For instance, the three open dots label an Al–Cr–Fe sample, with three different thicknesses of the oxide layer. Observe that, contrary to expectation, the reversible adhesion energy of water decreases with increasing thickness of the oxide layer as long as $t < 12$ nm.

surface contamination, resulting in a precise determination of the Al 3p density of states at the Fermi energy (denoted as $n_{Al\,3p}$ or n for short in the following). A subset of $n_{Al\,3p}$ data is presented in figure 6. Note that these values of $n_{Al\,3p}$ are obtained after proper calibration within an arbitrary scale that assigns the value $n_{Al\,3p} = 0.5$ to the pure fcc Al metal [17]. As a consequence, the nearly-free electron metal produces the largest possible value of $n_{Al\,3p}$ whereas for the compounds, $n_{Al\,3p}$ scales at lower values, with a marked minimum observed for the most complex compounds, i.e. quasicrystals. Another study [18] has shown that the partial density of Al s, d states at the Fermi energy is proportional to $n_{Al\,3p}$. Unfortunately, the 3d partial density of states of the TM constituent, which was also carefully measured using the same technique, cannot be related to $n_{Al\,3p}$, nor could any reliable total density of states be inferred from the partials owing to our lack of knowledge of the transition probabilities involved in the transition. We will therefore only rely upon data available for the Al 3p sub-band.

4. Results

We first test whether $W_{L \equiv H_2O}$ varies simply as a function of the chemical composition of the solid. Our raw data are summarized in figure 7, giving, on the one hand, the values of W_{H_2O} deduced from contact angle (equation (3)) as a function
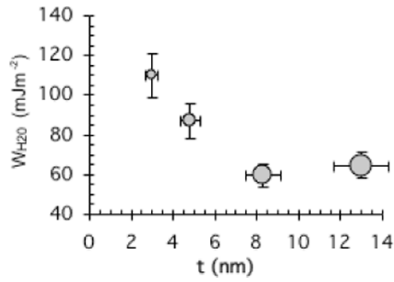
Figure 8. Reversible adhesion energy of water of a γ-brass Al–Cr–Fe sample equipped with its native oxide layer (smallest symbol) and supplementary layers of amorphous alumina (see text) of increasing thicknesses t (symbol size increases in proportion to t). W_{H_2O} decreases first, roughly in proportion to t^{-2}, until a crossover manifests itself at about $t = 12$ nm.

of the aluminium concentration in the samples (bottom part of the figure) and, on the other hand, the thickness of the oxide layer on each sample (inset). Each small symbol represents a different sample, either because the composition was varied or because it was prepared in a different run at identical composition. The data are scattered between the values for Teflon, and bulk alumina or window glass. Teflon sets the lower limit because it does not wet and displays the lowest possible value of W_{H_2O}. Conversely, alumina and, even more so, window glass show much larger values of W_{H_2O}, hence setting an effective upper limit that is close to the cohesive energy of water, $2\gamma_{H_2O} = 2 \times 72.8$ mJ m^{-2}. On the other hand, at $x = 100$ at.%, the value for an aluminium sample equals that of the bulk oxide. Even though there is no apparent correlation between Al content and W_{H_2O} for the rest of the samples, there is a trend in the data: the most perfect icosahedral quasicrystals are the closest to Teflon, whereas the simple crystalline compounds show values of W_{H_2O} two times larger.

Furthermore, and contrary to expectation, the reversible adhesion energy of water decreases with increasing thickness of the oxide layer. This is exemplified in figure 7 by using symbols, the size of which goes in proportion to the thickness t, see, for instance, the open dots that stand for an orthorhombic Al–Cu–Fe–Cr approximant. As a matter of fact, figure 8 shows that a crossover to the normal behaviour is recovered

for alumina layers thicker than 10–12 nm, in accordance with conventional literature, but below this limit, W_{H_2O} apparently goes in inverse proportion to some power of t (typically, t^{-2}). We will come back to this very important point in the forthcoming section.

Beyond this (for the moment) weak correlation, it is straightforward—using the several liquid methods introduced above (equation (5))—to realize that the LW component probed on the same set of samples is nearly independent from solid composition underneath the oxide layer (figure 9, left). Simultaneously, the AB contribution scales also with some power of $n_{Al\,3p}$ (figure 9, right). In particular, it vanishes right at the icosahedral quasicrystal composition, which is characterized by the smallest value of $n \equiv n_{Al\,3p}$ found in this system. Once more, this result cannot be inferred from standards of the literature on the subject. The partial Al 3p density of states deciphered from x-ray emission spectroscopy is a bulk property, which is probed, say, a few nanometres below the surface, whereas it is assumed till now that the wetting behaviour of a liquid is solely determined by electrostatic interactions taking place within the most external layers at the surface, within a range of a fraction of a nanometre. Experimental evidence, nevertheless, forces us to change our mind and seek for another interpretation.

The key correlation that does exist in the data is that W_{H_2O} scales linearly with the ratio $(n_{Al\,3p}/t)^2$, as shown in figure 10. The values of $n_{Al\,3p}$ are similar, but not necessarily identical, to the ones already published by Belin-Ferré *et al* [17] depending on sample preparation. (It should be kept in mind that the DOS data used here were obtained from the very same specimens as the ones used for the water droplet experiments.) As shown in figure 10, and within experimental accuracy, our W_{H_2O} data split into two branches, depending on the sample composition. The lower branch corresponds to Al–Cu–Fe specimens whereas the upper one relates to the Al–Cr–Fe(–Cu) system. Both converge to a common value on the y axis, within experimental accuracy.

The splitting into two branches can be understood if the wetting behaviour depends on the total DOS of the underlying metal at E_F (which is unavailable), rather than the partial Al 3p DOS (which we used). This is true because both Al 3p and hybridized 3d states are present at E_F. The contribution
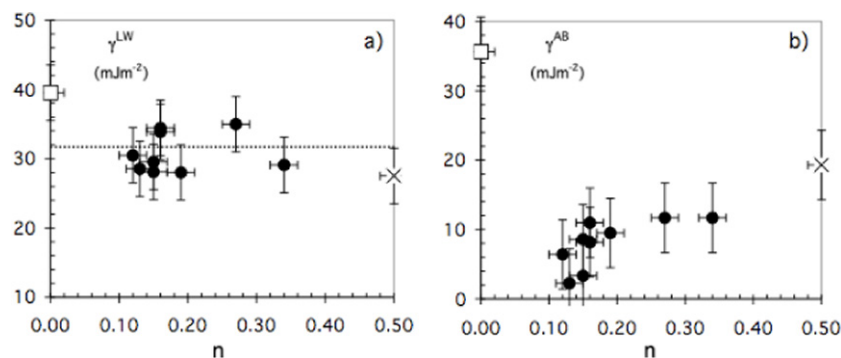

Figure 9. Lifshitz–van der Waals (a) and acid–base (b) components measured on Al-based intermetallics (solid dots, see text for details), crystalline alumina (square) and fcc aluminium (cross). The data are ordered on the x axis according to the density $n \equiv n_{Al\,3p}$ of Al 3p states at Fermi energy measured by x-ray emission spectroscopy [17] which is representative of the metallic character of the specimen (i.e. $n = 0.5$ in arbitrary units for a free electron metal like aluminium).
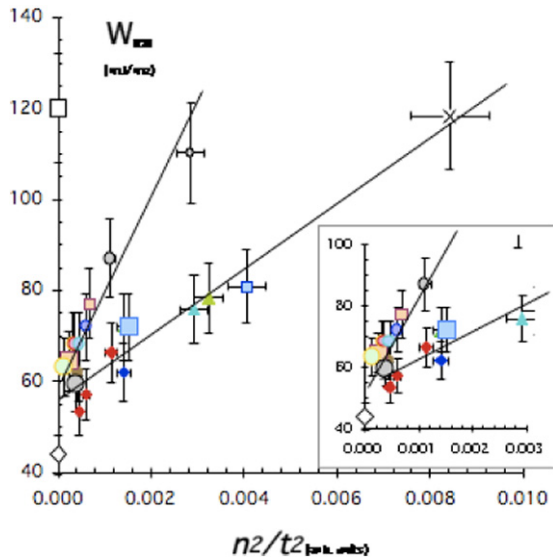
Figure 10. Variation of the reversible adhesion energy of water, W_{H_2O}, against $(n/t)^2$ where $n \equiv n_{Al\,3p}$ is the Al 3p partial DOS at E_F and t is the oxide thickness. The two straight lines are for specimens with different 3d-state contributions at E_F, as explained in the text. The line with the largest slope corresponds to Al–Cr–Fe(–Cu) samples whereas the other is for Al–Cu(–Fe) specimens. Open symbols located on the y axis are for Teflon (diamond) and alumina (square). They define, respectively, the lowest and largest values that can be observed with the present set of Al-based samples. The inset presents an enlargement of the data in the vicinity of $(n/t)^2$.

Figure 11. Sketch of the model used for the dipole–electron image force model. The oxide of thickness t defines the position of the z-axis origin, above which water dipoles sit at a distance equal or larger than d. Images are created beneath the oxide layer in the Fermi electron sea of density n. The distance at which these image dipoles are created in the bulk specimen depends on the electric permittivity of water and oxide, respectively, and amounts to $d + t\,\varepsilon_1/\varepsilon_2$, which is far larger than $d + t$.

of the Al 3p states, relative to the 3d states, is different in the Al–Cu–Fe system than in the Al–Cr–Fe(–Cu) system. More specifically, the difference between the two sets of data arises from a weak contribution of Fe 3d states at E_F in Al–Cu–Fe, but a stronger contribution of Cr and Fe 3d states in Al–Cr–Fe(–Cu). However, it has been shown [18] that the Al 3s, d and Al 3p DOSs are roughly proportional at E_F in each system separately, so that the Al 3p DOS still provides a good approximation of the variation of the total DOS, for each system independently.

In figure 9, using multiple-liquid experiments to probe a subset of these alloys, we have shown that the property of the solid that varies, within the framework established by equation (3), is I_{SL}^{AB}, not I_{SL}^{LW}. In particular, it turns out from this set of measurements that the Lifshitz–van der Waals component is nearly constant within experimental accuracy for all Al-based samples, with $\gamma_S^{LW} = 32 \pm 4$ mJ m^{-2}. Meanwhile, the same component is larger on crystalline alumina. In other words, the LW component is constant and can be disregarded in seeking to explain the data, leaving the AB component. Simultaneously, it is easy to infer from the convergence of the two linear sets of data in figure 10 that the same value of $\gamma_S^{LW} = 32$ mJ m^{-2} is responsible for the value of W_{H_2O} at $n^2/t^2 = 0$.

As already emphasized, a continuous change of the AB component of W_{H_2O} with the DOS is unexpected: AB interactions should not correlate with a bulk property, but should depend only on the outermost solid surface layer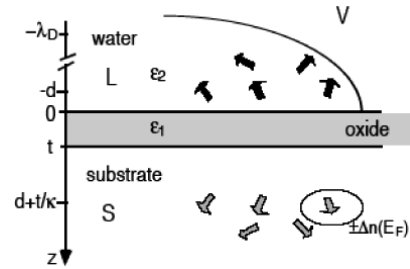s and their possible contamination. Therefore, they should vary erratically from one sample to another. Since this is not what we observe, we need to consider other possible types of interactions. An indirect coupling between θ and the DOS, via mechanical stress of the outermost oxide layer, itself determined by the epitaxial strain at the oxide–substrate interface, or a variation of the TM content of the alumina layer, is ruled out by the $t^{n\approx-2}$ dependence of W_{H_2O} that we observe experimentally (figure 8). Hence, our data strongly suggest that supplementary forces (different from true AB interactions) define the observed θ value.

5. Interpretation in terms of image forces

Let us now assume that we have deposited a minute droplet of water on the ideally flat surface of an oxide layer of thickness t. Water molecules carry a strong dipole $\bar{q}$ and experience long-range electrostatic forces over a distance at least equal to the Debye screening length λ_D. This distance is of the order of several tens of micrometers (typically 0.5 mm) in ultra-pure water that exhibits a very low density of charge carriers whereas $2 \leqslant t \leqslant 10$ nm. The charges located on a water molecule at a distance d from the oxide surface are able to generate image charges far away below the water–oxide interface (whose position defines the origin of the z coordinate taken along the normal to the interface, see figure 11). Following [19], we may approximate the solution to this problem by considering a system of plane waves emanating from the dipole and partially reflected at the water–oxide (hereafter w–o) and oxide–substrate (o–s) interfaces (figure 12). At this latter interface, reflection is total only for an ideally perfect conductor. In real alloys—and especially in quasicrystals–the electromagnetic field penetrates into the material to a depth proportional to the square root of the ratio between resistivity and frequency. In pure fcc Al, the penetration depth amounts to 10–12 nm at frequencies typical of the infrared range. Quasicrystals and approximants exhibit resistivities larger than that of the pure metal by 2–4 orders of magnitude, depending on lattice perfection and composition (complex Al-based intermetallics show intermediate values, the resistivity increasing with complexity of the unit cell).
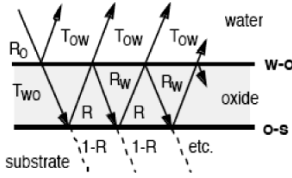
Figure 12. Explanation of the transmission and reflection coefficients used in the text, section 5.

Figure 13. Variation expected in arbitrary units for the image force component of the reversible adhesion energy of water when plotted against R (inset) or against n^2 ($n \equiv n_{\text{Al 3p}}$ in XES units) at constant unit thickness of the oxide layer and $\kappa = 0.12$, 0.18 and 0.24 (see the text).

Therefore, the penetration depth of the field is increased by 1–2 orders of magnitude in comparison to pure Al, i.e. well above the distance at which image dipoles form in the bulk of the material (see below). In such a situation, absorption of the wave is important and the reflection coefficient at the o–s interface is significantly smaller than the ideal value $R = 1$. Conversely, for a conventional metal like fcc aluminium with $R \geqslant 0.98$ in a broad range of frequencies, the wave does essentially not penetrate the substrate, which explains why wetting the oxidized metal is identical to wetting the bulk oxide.

Using the transmission coefficient from water to oxide and from oxide to water, respectively, as well as the reflection coefficients at the w–o interface, namely

$$T_{\text{wo}} = 2\varepsilon_1/(\varepsilon_1 + \varepsilon_2) \qquad T_{\text{ow}} = 2\varepsilon_2/(\varepsilon_1 + \varepsilon_2)$$

$$R_{\text{w}} = -\frac{\varepsilon_2 - \varepsilon_1}{\varepsilon_1 + \varepsilon_2} \qquad R_{\text{o}} = -\frac{\varepsilon_1 - \varepsilon_2}{\varepsilon_1 + \varepsilon_2} \qquad (8)$$

and introducing explicitly R in the equations of Jennings and Jones leads to an expression for the potential energy of a water molecule located at position d from the outermost surface given by

$$V(d) = -\frac{q}{16\pi\varepsilon_0} \frac{1}{d}\left[R_{\text{w}} + T_{\text{wo}}T_{\text{ow}}R\frac{1}{1 + t/d} \right.$$
$$+ R_{\text{o}}T_{\text{wo}}T_{\text{ow}}R^2\frac{1}{1 + 2t/d} + R_{\text{o}}^2T_{\text{wo}}T_{\text{ow}}R^3$$
$$\left. \times \frac{1}{1 + 3t/d} + \cdots \right] \qquad (9)$$

where ε_1 and ε_2 are, respectively, the dielectric permittivity of the oxide and of water and ε_0 the permittivity of vacuum. For small values of t, equation (9) is equivalent to

$$V(d) = -\frac{q}{16\pi\varepsilon_0} \frac{1}{d}[R_{\text{w}} + T_{\text{wo}}T_{\text{ow}}R(1 - t/d)$$
$$+ R_{\text{o}}T_{\text{wo}}T_{\text{ow}}R^2(1 - 2t/d) + \cdots]. \qquad (10)$$

Collecting successive powers of $1/d$ simplifies equation (10) to

$$V(d) = -\frac{q}{16\pi\varepsilon_0} \frac{[\varepsilon_1(1 + R) - \varepsilon_2(1 - R)]^2}{d[\varepsilon_1^2(1 + R)^2 - \varepsilon_2^2(1 - R)^2] + 4\varepsilon_1\varepsilon_2 Rt}. \qquad (11)$$

Since $\varepsilon_2 = 9.04$ F m^{-1} for water whereas $\varepsilon_1 \approx 1.1$ F m^{-1} for pure cubic alumina [20], it turns out that the ratio $\kappa = \varepsilon_1/\varepsilon_2$ is significantly smaller than 1. For an ideal conductor ($R = 1$), this means [19] that the centre of gravity of the image charges generated by the successive reflections at the w–o and o–s
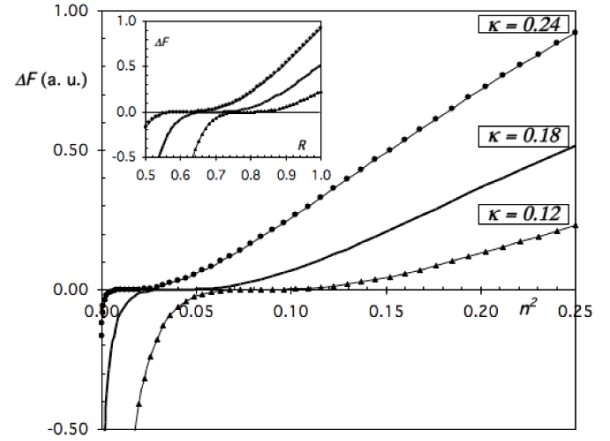
interfaces is translated towards the bulk substrate by a distance $d + t/k$. This effect, which is directly related to the strength of the water dipole, is very important in order to understand this specific wetting behaviour. Also, it tells us why wetting correlates with a bulk property like the DOS measured by XES and not to the local DOS at the o–s interface.

As long as the surface preparation technique avoids the formation of permanent charges and of dangling bonds at the surface of the (very thin) oxide layer, the only contribution to the surface free energy that arises from the oxide layer consists of a Lifshitz–van der Waals dispersive term, which is nearly independent of the value of t as soon as $t \geqslant 2$ nm [21]. We assign it the constant value of $\gamma_S^{\text{LW}} \approx 32$ mJ m^{-2} discussed earlier in this paper. To second-order level, the value of γ_S^{LW} should vary with the optical properties of the oxide layer depending on its TM content, its lattice perfection or density of defects, etc.

Therefore, the other contribution to the surface energy, which produces a permanent polarization of the water molecules, comes from the image electric field. According to classical electrostatics, the uncompensated image forces acting on the water molecules at the position of the three-phase line are proportional to $-\partial V/\partial z$ or, in a rough approximation and after proper integration over thermal statistical effects and distance from d to λ_{D}, to

$$E(0) = \frac{1}{16^2\pi\varepsilon_0} \frac{1}{t^2}[\kappa(1 + R)^2(\kappa(1 + R)^2 - 2(1 - R^2))$$
$$- \kappa^{-1}(1 - R)^2 \times (\kappa^{-1}(1 - R)^2 - 2(1 - R^2))]/R^2. \qquad (12)$$

The forces that stretch the three-phase line are thus essentially proportional to the term between brackets (divided by R^2, which limits the validity range of equation (12) to metallic substrates) and inversely proportional to the square of the thickness, in accordance with figure 8 for $t < 12$ nm. The inset of figure 13 presents the variation of this term labelled in the following $F = [\cdots]/R^2$ (see equation (12)) as a function of R for three values of κ, namely $\kappa = 0.12$, as expected for a

layer of pure, cubic alumina and two slightly larger values $\kappa = 0.18$ and 0.24, which correspond better to amorphous alumina that dissolves a small amount of transition metals and exhibit very small, but finite, electronic conductivity. The low-R region of the diagram that goes with negative image forces may not be meaningful because it corresponds to a regime in which absorption of the wave by the substrate dominates. Note that $F = 0$ is taken for $W_{H_2O} = 2\sqrt{\gamma_S^{LW}\gamma_{H_2O}^{LW}} = K_{H_2O}^{LW} = \text{constant}$ since $\gamma_S^{LW} = 32\ \text{mJ m}^{-2}$ is independent of the substrate nature.

In order to understand further figure 10, one needs to know the relationship between R and the DOS in metallic alloys. There is very little published so far in the literature on this topic and one has to guess an empirical relationship. From infrared spectroscopy experiments [22], we know that $R \approx 0.6$ at low frequencies in high quality quasicrystals (whereas $n_{Al\ 3p} \approx 0.12$ in XES units [17]). R is larger in approximants and crystals of similar composition (with $n_{Al\ 3p}$ in the range 0.14–0.4). Meanwhile, $R = 1$ in fcc Al as for an ideal conductor (when $n_{Al\ 3p} = 0.5$). Hence, a simple linear relationship between R and $n_{Al\ 3p}$ is

$$R = \frac{n_{Al\ 3p}^f + n_{Al\ 3p}}{2n_{Al\ 3p}^f} = \frac{1+2n}{2} \tag{13}$$

where $n_{Al\ 3p}^f$ represents the Al 3p DOS at E_F in a free electron system like fcc Al and the transformation $2n_{Al\ 3p}^f = 1$ sets the right-hand part of equation (13) to XES units adapted to the Al 3p partial DOS. The values of ΔF, as defined above, are represented in figure 13 as a function of n^2 ($n \equiv n_{Al\ 3p}$ in XES units). The obtained variation of ΔF versus n^2 (at $t = \text{unity}$) is indeed essentially linear in the range spanned by our experimental values ($n_{Al\ 3p} \geqslant 0.12$), which fits nicely with the experimental evidence pointed out in figure 10.

Then, equation (4) may be rewritten:

$$W_{H_2O} = K_{SL}^{LW} + K^{im}n^2/t^2 \equiv I_{SL}^{LW} + I_{SL}^{im}. \tag{14}$$

The image force contribution labelled I_{SL}^{im} in equation (14) plays a role similar to the Lewis acid–base component (I_{SL}^{AB} in equation (4)), but with quite a different meaning. Yet, an AB component I_{SL}^{AB} should be added to the right-hand side of equation (14) if such interactions are still present at the surface. Our surface preparation method allowed us to cancel out all AB interactions, which in turn made the contribution from image forces visible. Usually, AB components to the surface energy hide the I_{SL}^{im} contributions since they are of comparable strength, but vary erratically with the surface preparation process.

6. Conclusion

By expanding and exploring a simple comparison quantitatively across many different Al-based intermetallics, we have arrived at the main result emphasized in this paper: the degree to which water wets metals covered by an amorphous oxide depends directly on the density of conduction states in the bulk, and inversely on the oxide layer thickness, for thin enough layers. This result could not have been anticipated from the accepted understanding of the wetting of aluminium oxides by water. The existing paradigm would have predicted that the key interactions are *very localized* at the liquid–solid interface (aside from the dispersive forces, which we showed to be irrelevant because they add a constant contribution that depends only on the nature of the covering oxide). Our results, however, imply that the key interactions are the longer-range forces between water molecules and their image dipoles, and hence wetting probes the properties of the metal beneath the oxide film, provided that the oxide is thin enough. We have shown that the established paradigm still applies for sufficiently thick oxide layers, where a crossover to the expected behaviour of the bulk oxide is achieved.

The reason why no charges are trapped or no polar contribution rises at the very surface of these specific materials is most probably related to the amorphous structure of the oxide. Further work is in progress to clarify this point. Nevertheless, we feel our data sheds new light on the wetting of oxidized alloys by a strongly polar liquid like water.

References

[1] Israelachvili J 1985 *Intermolecular and Surface Forces* (London: Academic)
de Gennes P G 1985 *Mod. Phys.* **57** 827
Tyson W R 1975 *Can. Metall. Q.* **14** 307
Carré A 1989 *Phénomènes d'Interface* ed J Briant (Paris: Technip)
[2] Young T 1805 *Trans. R. Soc.* **95** 65
[3] Dubois J M and Weinland P 1993 *French Patent Specification* 2635117
Dubois J M and Weinland P 1993 *US Patent Specification* 5204191
[4] Dubois J M 2005 *Useful Quasicrystals* (Singapore: World Scientific)
[5] Belin-Ferré E and Dubois J M 2006 *Int. J. Mater. Res.* **97** 985
[6] Good R J 1992 *J. Adhes. Sci. Technol.* **6** 1269
[7] Dubot P, Cenedèse P and Gratias D 2003 *Phys. Rev.* B **68** 033403
[8] Rivier N 1993 *J. Non-Cryst. Solids* **153/154** 458
[9] Tsai A P, Inoue A and Masumoto T 1989 *Mater. Trans. JIM* **30** 463
Tsai A P, Niikura A, Inoue A, Masumoto T, Nishida Y, Tsuda K and Tanaka M 1994 *Phil. Mag. Lett.* **70** 169
Sato T J, Abe E and Tsai A P 1997 *Japan. J. Appl. Phys.* **36** L1038
[10] Quiquandon M, Quivy A, Devaud J, Faudot F, Lefebvre S, Bessière M and Calvayrac Y 1996 *J. Phys.: Condens. Matter* **8** 2487
Dong C and Dubois J M 1991 *J. Mater. Sci.* **26** 1647
[11] Black P J 1955 *Acta Crystallogr.* **8** 43
Bown M G and Brown P J 1956 *Acta Crystallogr.* **9** 911
see also Fournée V, Belin-Ferré E and Dubois J M 1998 *J. Phys.: Condens. Matter* **10** 4231 for more details about this crystalline samples
[12] Demange V, Wu J S, Brien V, Machizaud F and Dubois J M 2001 *Mater. Sci. Eng.* **294–296** 79

[13] Brunet P, Zhang L, Sordelet D J, Besser M and Dubois J M 2000 *Mater. Sci. Eng.* **294–296** 74

[14] Gil-Gavatz M, Rouxel D, Pigeat P, Weber B and Dubois J M 2000 *Phil. Mag.* A **80** 2083
Weisbecker P, Bonhomme G, Bott G and Dubois J M 2005 *J. Non-Cryst. Solids* **351** 1630

[15] Bonhomme G, Lemieux M, Weisbecker P, Tsukruk V V and Dubois J M 2004 *J. Non-Cryst. Solids* **334/335** 532

[16] Strohmeier B R 1990 *Surf. Interface Anal.* **15** 51

[17] Belin-Ferré E, Fournée V and Dubois J M 2000 *J. Phys.: Condens. Matter* **12** 8159

[18] Belin-Ferré E, Fournée V and Dubois J M 2001 *Mater. Trans. JIM* **42** 911

[19] Jennings P J and Jones R O 1988 *Adv. Phys.* **37** 341

[20] Weaver J H and Frederikse H P R (ed) 1994 *Handbook of Chemistry and Physics* 75th edn (Boca Raton, FL: CRC Press)

[21] Miller W J and Abbott N L 1997 *Langmuir* **13** 7106

[22] Demange V *et al* 2002 *Phys. Rev.* B **6** 144205